Ultrathin Ni nanowires embedded in $SrTiO_3$: Vertical epitaxy, strain relaxation mechanisms, and solid-state amorphization

X. Weng,[1] M. Hennes,[1] A. Coati,[2] A. Vlad,[2] Y. Garreau,[2,3] M. Sauvage-Simkin,[2] E. Fonda,[2] G. Patriarche,[4] D. Demaille,[1] F. Vidal,[1] and Y. Zheng[1]

[1]*Sorbonne Université, CNRS, Institut des NanoSciences de Paris, INSP, F-75005 Paris, France*

[2]*Synchrotron SOLEIL, L'Orme des Merisiers Saint-Aubin BP 48, 91192 Gif-sur-Yvette Cedex, France*

[3]*Université Paris Diderot, Sorbonne Paris Cité, MPQ, UMR 7162 CNRS, Bâtiment Condorcet, Case courrier 7021, 75205 Paris Cedex 13, France*

[4]*Centre de Nanosciences et de Nanotechnologies (C2N), CNRS, Université Paris Sud, Université Paris Saclay, F-91460 Marcoussis, France*

(Received 19 July 2018; published 11 October 2018)

Strain is a key parameter affecting the physical properties of heterostructured thin films and nanosized objects. Generally, the design of application-optimized hybrid structures requires good structural compatibility between the involved phases. However, when controlled appropriately, lattice mismatch can turn from a detrimental to a beneficial property, enabling further functionality tuning. Due to their large heterointerface, nanocolumnar composites are an ideal test bed for such strain engineering approaches, but coupling mechanisms at vertical interfaces are still poorly understood. In the present paper, we therefore present a detailed analysis of ultrathin Ni nanowires, with diameters between 1.7 nm and 5.3 nm, vertically epitaxied in a $SrTiO_3/SrTiO_3(001)$ matrix. Using a combination of x-ray diffraction (XRD), high resolution transmission electron microscopy (HRTEM), and x-ray absorption spectroscopy (XAS) measurements, we unveil peculiar structural features of this hybrid system. We show that the axial deformation of the nanowires depends on their diameter and that their radial strain differs sensitively from the value expected when considering the Poisson ratio. We also provide evidence for the existence of a relaxation mechanism consisting in a slight tilting of crystallographic nanowire domains which reduces the misfit at the Ni-$SrTiO_3$ heterointerface. This, in turn, induces significant structural disorder and results in a successive amorphization of the metallic phase upon diameter reduction of the nanowires.

DOI: 10.1103/PhysRevMaterials.2.106003

I. INTRODUCTION

In thin films, strain, which arises from the lattice mismatch at heterointerfaces, can be used as a powerful lever to engineer selected material properties, such as ferroelectricity [1], magnetic anisotropy [2,3], or superconductivity [4]. There are, however, some limits to this approach: The deposited layers have to be thin enough to avoid lateral strain relaxation via formation of misfit dislocations, and the choice of materials with large mismatch values often results in thin films with poor epitaxial quality.

In recent years, the synthesis of vertically assembled nanocomposites (VAN) has been proposed as a new strategy to overcome limitations encountered in planar systems [5–19]. VANs are made of two phases that grow epitaxially with each other on a common substrate, resulting in nanowires (NWs) of a given material embedded in a matrix of another material, as sketched in Fig. 1. From a structural perspective, the involved phases in these columnar composites "work synergistically" [17], resulting in an improved crystallinity [20]. Due to the misfit at the vertical heterointerface, huge vertical strains (ϵ_{zz}) can be induced in the embedded structure for thicknesses beyond values commonly observed for the critical thickness in planar heterostructures. This has indeed been used in order to tailor the properties of VANs of interest in different fields [17].

To achieve thorough control over the nanocomposite architecture, an improved understanding of structural coupling and relaxation mechanisms at vertical heterointerfaces is required. Recent studies have, for example, unraveled peculiar behaviors in embedded nanopillars and wires, exhibiting exotic auxeticlike strain states [18]. The prominent role played by dislocations and possible strategies to achieve maximum ϵ_{zz} values, ultimately linked to the vertical coherent interfacial area, were also addressed recently [19]. However, in contrast to planar systems, strain relaxation mechanisms in vertical epitaxy remain generally less well understood.

Simple considerations on the balance between the interface energy, that scales as the diameter of the pillars and the elastic energy, scaling as the square of the diameter, indicates that ϵ_{zz} should increase as the diameter decreases. It is thus interesting to explore the evolution of the strain state in the NWs as the diameter decreases. In this respect, metal-ceramic VANs [6,21–32] are promising model systems because they offer the possibility to control the diameter of the nanowires in the few nanometers range. In the present paper, we investigate vertical epitaxy and strain states in VANs composed of Ni NWs in $SrTiO_3/SrTiO_3(001)$ epilayers. The lattice mismatch between Ni and STO is quite large (about 11% for $a_{Ni} = 3.524$ Å and $a_{STO} = 3.905$ Å) [33] and axial strain up to 3.9% can be achieved in Ni NWs. This naturally raises questions on the mechanisms at play to relax strain partially in the system

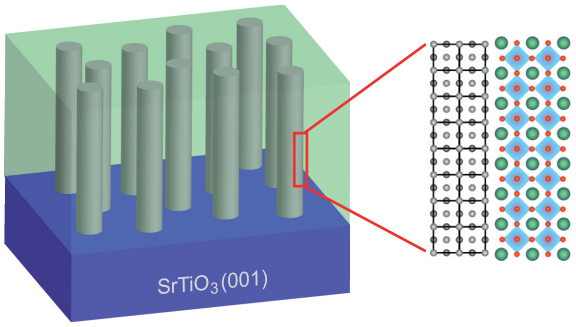

FIG. 1. Schematics of vertically assembled epitaxial Ni wires embedded in a $SrTiO_3$ matrix, with crystallographic structures of Ni and $SrTiO_3$.

and on the structure of the NWs in the ultrathin limit. We address these issues by a combined x-ray diffraction and x-ray absorption spectroscopy study of the structure of ultrathin Ni NWs.

II. SAMPLE GROWTH AND ANALYSIS

A. Growth

Following procedures established previously to synthesize Co, Ni, and Co_xNi_{1-x} nanowires in $CeO_2/SrTiO_3$ and (Sr, Ba)TiO_3 [21–29], Ni nanowires were grown by sequential pulsed laser deposition (PLD) of nickel and $SrTiO_3$ (STO) on $SrTiO_3$(001) substrates, using a quadrupled Nd:YAG laser (wavelength 266 nm) operating at 10 Hz and a fluence in the 1–3 J/cm^2 range. The temperature of the substrate during growth was about 650 °C. Two PLD setups were used to obtain a series of 10 samples: (i) One setup is kept under ultrahigh vacuum conditions and the samples will be labeled 1-U to 5-U hereafter. (ii) The second setup is under secondary vacuum conditions with a base pressure in the 10^{-6} mbar range during growth; samples will be referred to as 6-S to 10-S in what follows.

In both cases, the growth process consists in the repetition of one basic deposition sequence alternating laser shots on STO and NiO targets. Labeling n_{Ni} and n_{STO} the number of laser shots on Ni and STO targets in a basic sequence, the (n_{Ni}, n_{STO}) sequence is repeated N times. Each basic sequence deposited about 0.05 nm of STO matrix for samples 6-S to 9-S and 0.3 nm for 1-U to 5-U. The amount of Ni deposited in a sequence was about one order of magnitude less than that of STO for both cases. The sequential deposition scheme introduces dead times, corresponding to target movements, during which no deposition occurs. The impact of n_{Ni}, n_{STO}, deposition rate, and dead time on the growth has been studied in Ref. [30]. Combining experiments and kinetic Monte-Carlo simulations, the influence of the growth parameters on the value of NWs areal density ρ and mean diameter $\langle D \rangle$ was studied. One salient feature of the sequential deposition scheme used here is that, for a fixed value of n_{Ni}, $\langle D \rangle$ will vary as $(n_{Ni}/n_{STO})^{1/2}$ in the density range explored. Following the sequential deposition step, the samples are capped with a ~ 3 nm thick pure STO layer in order to protect them against contamination and avoid NW oxidation.

B. Structural measurements

The structure of the samples was studied using a combination of techniques including transmission electron microscopy (TEM) and scanning transmission electron microscopy (STEM), x-ray diffraction (XRD), and x-ray absorption spectroscopy (XAS). High resolution transmission electron microscopy (HRTEM) data were acquired using a JEOL JEM 2100F equipped with a field-emission gun operated at 200 kV and a Gatan GIF spectrometer. STEM data were acquired using a Titan Themis 200. Energy-dispersive x-ray spectroscopy (EDX) was used to map the chemical distribution of the elements in the samples in plan-view geometry. XRD data were collected on a laboratory 5-circles diffractometer (Rigaku SmartLab) with Cu K_α radiation (wavelength of 1.54 Å) in order to determine the epitaxial relationship in the nanocomposites and the mean axial strain in the Ni wires. In order to gain detailed insight into the strain states of the nanowires, reciprocal space mapping (RSM) was performed at the SixS beamline of synchrotron SOLEIL with 18.4 keV monochromatic radiation (wavelength of 0.674 Å). Throughout this paper, the reciprocal coordinates $hk\ell$ refer to the reciprocal lattice units (r.l.u.) of the cubic STO substrate with a lattice parameter of 0.3905 nm. The growth direction is defined as STO [001]. The nanowire long axis is parallel to this direction.

X-ray absorption near-edge spectroscopy (XANES) data were collected at the Ni K-edge at the SAMBA beamline of Synchrotron SOLEIL. The samples were probed in fluorescence detection mode. The K_α fluorescence yield of Ni was monitored by a 36 pixels monolithic Germanium detector (Canberra France). Opting for fluorescence mode detection enabled us to probe the Ni content of the whole nanocomposite epilayers. Structural anisotropy in the NWs was assessed by linear dichroism (LD) analysis. Therefore, all XAS measurements were performed in two different configurations $\mathcal{L}_\perp$ and $\mathcal{L}_\parallel$, with $\phi = 15°$ and $\phi = 75°$, respectively, ϕ representing the angle between the incoming beam and the surface normal of the sample. In the $\mathcal{L}_\perp$ configuration, the x-ray electric field polarization vector thus had its dominant component aligned perpendicularly to the NWs. In turn, the $\mathcal{L}_\parallel$ configuration allowed us to probe the nanowire structure with the x-ray electric field polarization along the nanowire axis.

III. EPITAXY AND STRAIN OF Ni NANOWIRES

A. Diameter, density, and chemical composition

We first report on the formation of Ni nanowires and on their general structural features. The sequential deposition scheme leads to the vertical self-assembly of NWs as described schematically in Fig. 1 and already observed previously in other metal/ceramic nanocomposites. Figure 2(a) shows a low resolution bright-field plan view micrograph of sample 4-U, unveiling the presence of a dense NW assembly. From the statistical analysis of several such images, the diameter distribution is retrieved. It is shown in Fig. 2(b) for sample 4-U, where a unimodal distribution can be seen, with a mean value of the diameter $\langle D \rangle = 2.2$ nm and a full width at half maximum on the order of 25% of the value of $\langle D \rangle$.

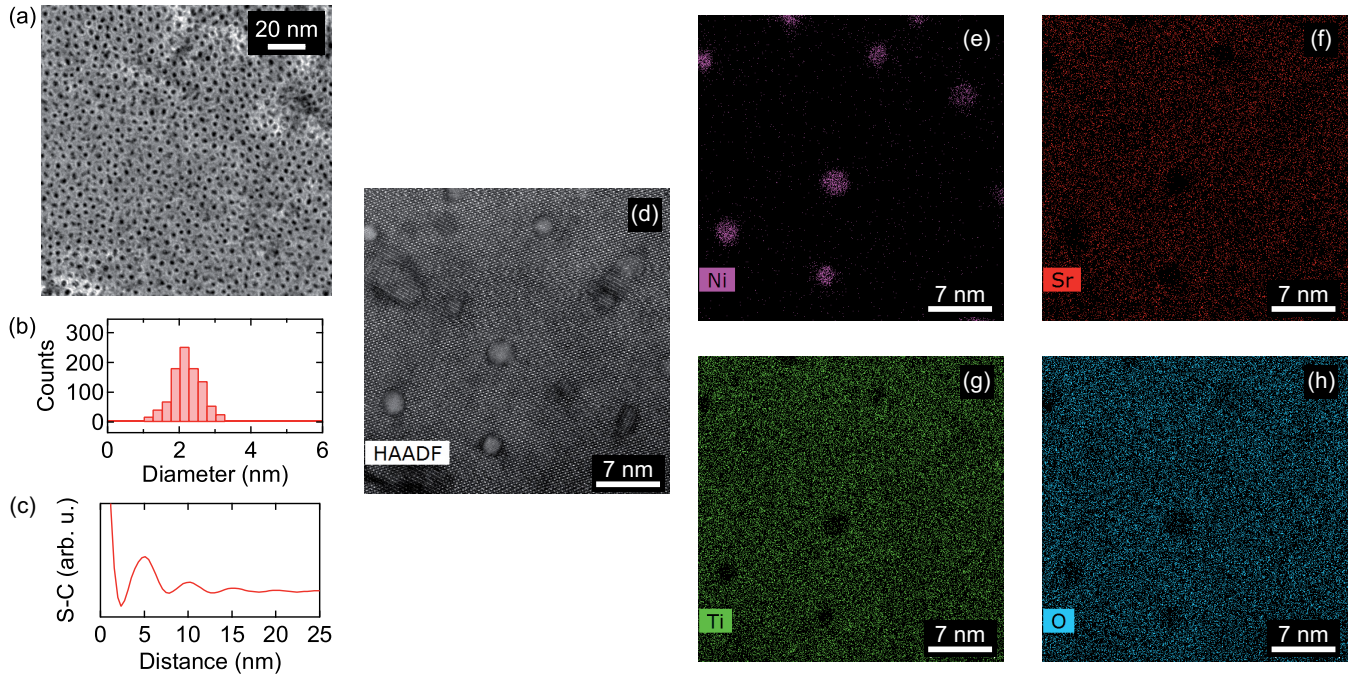

FIG. 2. (a) Low resolution plan view TEM image of Ni nanowires embedded in a $SrTiO_3$ matrix (sample 4-U). (b) Diameter distribution of Ni nanowires as extracted from TEM images such as the one displayed in (a). (c) Line profile obtained from the self-correlation of (a), with oscillations enabling us to extract the mean distance between wires. (d) STEM-HAADF plan view of Ni nanowires, sample 7-S. (e)–(h) Chemical maps obtained by EDX in the same region as the one in (d). (e) Ni map, (f) Sr map, (g) Ti map, and (h) O map.

Such a kind of distribution was observed in every sample with $\langle D \rangle$ varying in the 1.7–5.3 nm range, depending on the growth sequence used. The areal density ρ of the NWs can also be extracted from such TEM measurements in plan view geometry. Self-correlation of images such as the one displayed in Fig. 2(a) can also be used to extract the average distance between nearest neighbor NWs. Figure 2(c) shows a profile of the self-correlation with clear 5 nm period oscillations, indicating that the mean distance between NWs is 5 nm in sample 4-U. Results of the measurements of $\langle D \rangle$ and ρ for the whole set of samples are given in Table I. Finally, cross-sectional TEM analysis shows that the length of the wires is equal to the thickness of the epilayer.

TABLE I. Structural parameters deduced from TEM and XRD analysis of the nanocomposites. $\langle D \rangle$: mean diameter of the NWs, ρ: in-plane density of the NWs, t: epilayer thickness, $\langle \epsilon_{zz} \rangle$: mean axial strain.

Sample	$\langle D \rangle$ (nm)	ρ (cm^{-2})	t (nm)	$\langle \epsilon_{zz} \rangle$ (%)
1-U	1.7	$3.0\ 10^{12}$		
2-U	1.8	$4.5\ 10^{12}$	62	
3-U	1.9	$5.8\ 10^{12}$	125	3.9
4-U	2.2	$4.4\ 10^{12}$	59	3.6
5-U	2.5	$3.9\ 10^{12}$	77	3.4
6-S	1.7	$7.8\ 10^{11}$		
7-S	2.4	$5.9\ 10^{11}$	139	3.6
8-S	4.1	$1.8\ 10^{12}$	231	3.2
9-S	4.5	$4.2\ 10^{11}$	74	2.8
10-S	5.3	$4.1\ 10^{11}$	51	2.3

In addition to our analysis of nanowire size and density, we scrutinized the chemical composition of the wires by performing STEM-HAADF imaging and EDX-mapping of Sr, Ti, O, and Ni. Figures 2(d)–2(h) show an exemplary plan-view map of sample 7-S. Ni nanowires can easily be identified in the Z-contrast image and their location correlates with spots of high Ni concentration. Quantitative analysis of the data shows almost complete absence of Ni in the surrounding $SrTiO_3$ with $c(\mathrm{Ni}) < 0.25\,\mathrm{at\%}$ ($c(\mathrm{Ni}) + c(\mathrm{Sr}) + c(\mathrm{Ti}) + c(\mathrm{O}) = 1$). In contrast, we observe small, albeit non-negligible matrix component concentrations when analyzing single NWs. For example, $c(\mathrm{Ti}) = 6.7 \pm 2.7\,\mathrm{at\%}$, $c(\mathrm{Sr}) = 2.8 \pm 2.2\,\mathrm{at\%}$, and $c(\mathrm{O}) = 25.8 \pm 6.9\,\mathrm{at\%}$ is obtained when averaging over the NWs shown in Fig. 2(d). We stress here that large relative errors result from the small volumes probed when restricting the analysis region to single ultrathin NW. Within measurement uncertainty, the aforementioned data are roughly compatible with $SrTiO_3$ stoichiometry. This shows that Sr, Ti, and O contributions to the EDX signal coming from single NWs arise from the presence of the $SrTiO_3$ capping layer covering the thin film, rather than from incorporation of minute amounts of these elements into the nanowires. The metallic nature of Ni within the NWs is further substantiated by spectroscopic data obtained at the Ni K edge shown in Sec. III D of this paper. Titanium is known to favor oxygen scavenging at oxide interfaces [34]. In the present case, the NiO reduction is attributed to oxygen scavenging by $SrTiO_3$.

To summarize these results, our structural and chemical analysis demonstrates full phase separation between Ni and $SrTiO_3$ and self-assembly of nanowires with tunable $\langle D \rangle$ in the 1.7–5.3 nm range as a function of the growth conditions. This allows us to study the effect of diameter reduction on

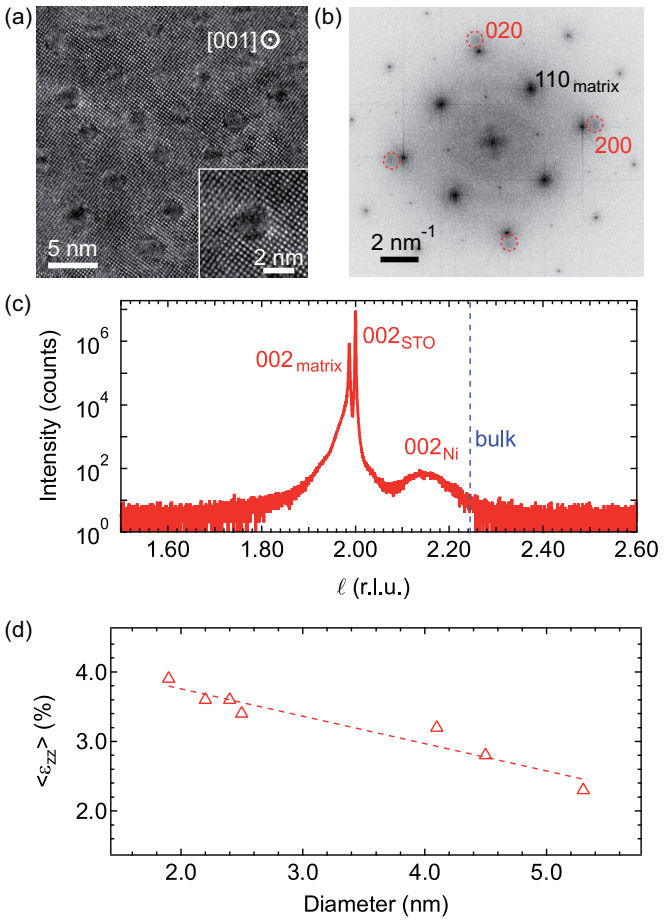

FIG. 3. (a) High resolution plan view TEM image of Ni nanowires in $SrTiO_3$ matrix; inset: zoom on a single nanowire (sample 4-U). (b) FFT of image (a) evidencing the in-plane epitaxial relationship between Ni and $SrTiO_3$. (c) θ-2θ scan of sample 8-S. The abscissa is in $SrTiO_3$ reciprocal lattice unit (r.l.u.). The vertical dashed line indicates the position of the 002 peak for unstrained nickel. (d) Mean axial strain, as deduced from θ-2θ scans, for samples with different diameters.

epitaxy and structure of elemental Ni NWs embedded in $SrTiO_3/SrTiO_3(001)$. Furthermore, the comparison of U and S samples with similar diameters but grown under distinct atmospheres allows us to address the impact of the oxygen partial pressure on the structure of the NWs.

B. Vertical epitaxy and average axial strain

The epitaxial character of the samples was examined using HRTEM and XRD measurements. Figure 3 shows typical measurements obtained for two samples of the series. From data presented in Figs. 3(a) and 3(b), obtained along the [001] zone axis, a cube-on-cube epitaxy of face-centered cubic Ni in the $SrTiO_3$ matrix can be deduced. Figure 3(b) shows a diffraction pattern obtained by applying a fast Fourier transform (FFT) to the HRTEM image. The 200 and 020 spots of Ni, highlighted by circles, are aligned with the 200 and 020 spots of the matrix. The cube-on-cube epitaxy is further confirmed by XRD θ-2θ scans, probing the out-of-plane epitaxial alignment. As shown in Fig. 3(c), the 002

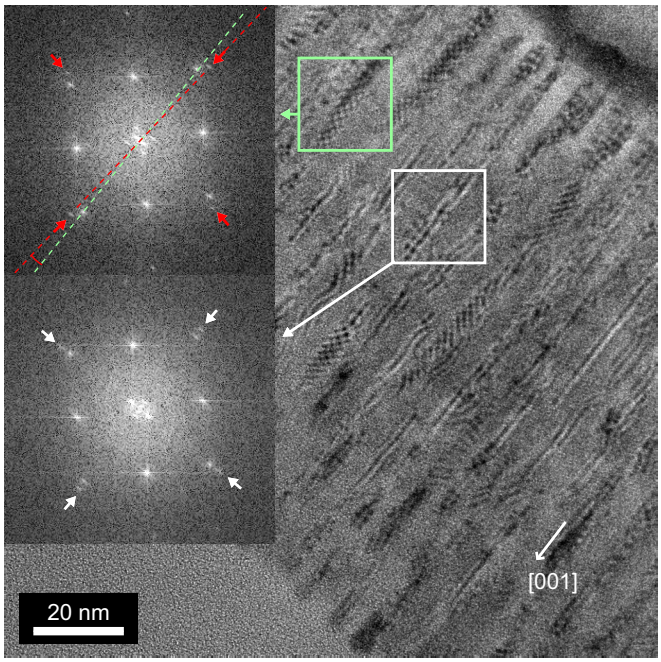

FIG. 4. Cross section TEM image of Ni nanowires in $SrTiO_3$ matrix (sample 8-S); insets: FFT of selected areas delimited by light squares. The inset at the top evidences the local misorientation α of the Ni lattice with respect to the $SrTiO_3$ lattice.

reflection of Ni is observed in agreement with the epitaxial relationship deduced from TEM measurements. It should be noted that the out-of-plane lattice parameter of the matrix is slightly larger than that of the substrate, as shown by the peak at $\ell < 2$. This is a well-documented consequence of the nonstoichiometry of $SrTiO_3$ when growth is carried out in an oxygen free atmosphere [35–37].

A peculiar feature of the Ni NWs is their strain state. The average axial strain, denoted $\langle\epsilon_{zz}\rangle$ in what follows, reaches several percent, as reflected by the low ℓ value of the 002 peak position with respect to the value expected for relaxed bulk Ni, see Fig. 3(c). This is a consequence of the epitaxy and the value of $\langle\epsilon_{zz}\rangle$ reflects the balance between the interface energy and the elastic energy stored in the NWs. Consistently with such balance, we observe a decrease of $\langle\epsilon_{zz}\rangle$ when the diameter increases, as shown in Fig. 3(d). The strain reaches fairly large values (up to 3.9% at 1.9 nm diameter, see Table I) that could be exploited to tailor the magnetic properties through the magnetoelastic anisotropy.

The FFT obtained from plan view TEM images gives patterns that contain information on an assembly of wires. From the large width of the 002 Ni peak, one can suspect that there is some degree of crystalline disorder in Ni. This is indeed confirmed by HRTEM cross-sectional imaging of the nanowires. As shown in Fig. 4, the structure of the wires is not homogeneous. The presence of the embedded NWs, oriented along the growth direction, gives rise to Moiré patterns arising from multiple diffraction events in cross-sectional geometry. Such patterns are seen to vary when moving along the [001] direction. This indeed reflects the fact that there is some misorientation of Ni with respect to the perfect cube-on-cube epitaxy and that the misorientation varies axially. Selected

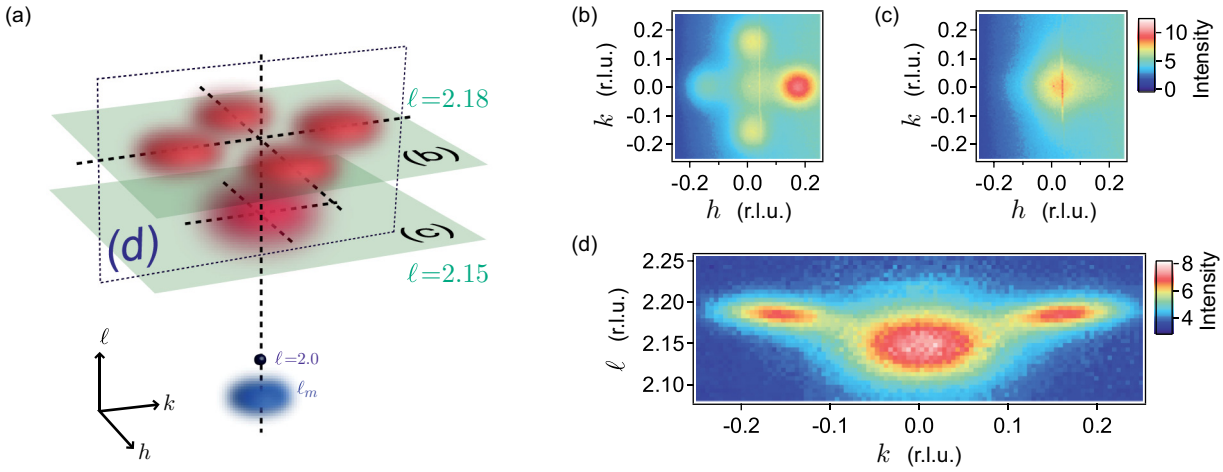

FIG. 5. RSM of sample 8-S. (a) Sketch of the diffraction diagram in the reciprocal space in the vicinity of the 002 reflections. r.l.u. refers to $SrTiO_3$ reciprocal lattice. The reflection of the $SrTiO_3$ substrate is located at $\ell = 2$. ℓ_m: coordinate of the reflection from the matrix. The 002 reflection of Ni is composite, with a spot at $h = k = 0$, $\ell = 2.15$ and four spots in the $\ell = 2.18$ plane, at $h = \pm 0.1575$ and $k = \pm 0.1575$. Planes labeled (b)–(d) correspond to the cuts of the reciprocal space shown in panels (b)–(d) of the figure. (b) Cut of the reciprocal space in the $\ell = 2.18$ plane. (c) Cut of the reciprocal space in the $\ell = 2.15$ plane. (d) Cut in the $h = 0$ plane.

area diffraction patterns, obtained by performing FFTs, are shown in the insets of Fig. 4. These patterns can be indexed by considering a slight rotation by an angle α of $[001]_{Ni}$ with respect to the [001] direction of the matrix. The upper pattern corresponds to $\alpha = 4^\circ$ and the lower one to $\alpha = 0$. This indicates that the epitaxial relationship is not as simple as initially deduced from symmetrical θ-2θ scans. Indeed, given the large width of the Ni 002 peak in θ-2θ scans, such an inhomogeneity is not surprising.

C. Strain relaxation mechanisms

In order to characterize the inhomogeneous structure of the Ni nanowires, extensive reciprocal space mapping was carried out using synchrotron x-ray diffraction. These measurements revealed the composite nature of the low index diffraction peaks related to Ni. As an example, Fig. 5(a) gives a sketch of the Ni 002 peak in sample 8-S as deduced from measurements: A central peak at $\ell = 2.15$ and $h = k = 0$ is observed, accompanied by four tilted spots at $\ell = 2.18$ and $h = \pm h_s$ with $k = 0$ or $k = \pm h_s$ and $h = 0$, with $h_s = 0.1575$. This is demonstrated by slices of the reciprocal space displayed in Figs. 5(b) and 5(c), where this composite peak is cut by two high symmetry orthogonal planes. In a constant ℓ plane, the central peak and the four tilted spots along [100] and [010] can be clearly observed. We underline the fact that we mapped the full region of the reciprocal space, confirming this composite structure of Ni 002. The difference in intensity between the peaks in the $\ell = 2.18$ plane is simply related to the variation of the x rays incidence angle during data acquisition and the consequent variation of the probed volume. The irradiated volume scales as $1/\sin\omega$, with ω the incidence angle. The Bragg angle θ_B for the central peak at $h = k = 0$ is 10.84°. The peaks at $h = \pm h_s$ are tilted by $\alpha = \pm 4^\circ$. Therefore, the intensity of the peak at $h = h_s$ is larger than the intensity at $h = -h_s$ by a factor $\sin(\theta_B + \alpha)/\sin(\theta_B - \alpha) = 2.15$. Experimentally, we measure a factor 2 for this intensity ratio, in very good agreement. The tilted spots have thus the same intensity and the fourfold symmetry of the system is not broken.

The width of the spot can be determined by fitting line profiles such as the ones displayed in Fig. 6 obtained for one of the fourfold degenerated spots at $|h|$ or $|k| = 0.1575$ in the $\ell = 2.18$ plane. From the width along k, $\Delta k = 0.1115$, Fig. 6(a), a radial coherence length of 3.5 nm is deduced. This value is quite close to the mean value of the diameter of the NWs in this sample, $\langle D \rangle = 4.1$ nm. The situation is different when considering the coherence along ℓ. From Fig. 6(b), a width $\Delta\ell = 0.0311$, giving an axial coherence length $L_{\text{coh}} = 12.6$ nm, is extracted. This is significantly smaller than the

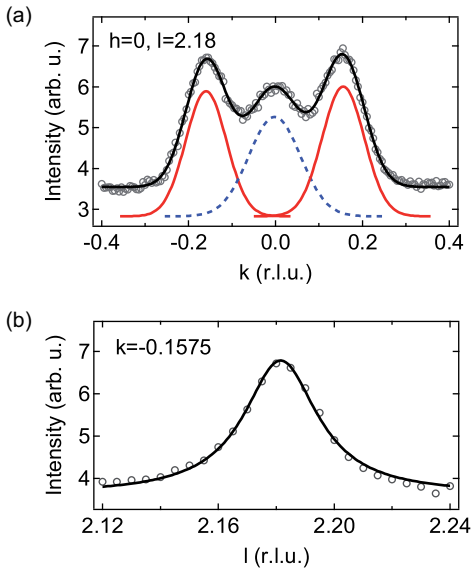

FIG. 6. (a) Profile of diffracted intensity along k for $h = 0$ in the $\ell = 2.18$ plane, obtained from data in Fig. 5(b). The component at $k = 0$ (dashed line) originates from the broad peak at $\ell = 2.15$, see Fig. 5(d). (b) Profile of diffracted intensity along ℓ for $k = -0.1575$ and $h = 0$, obtained from data in Fig. 5(d).

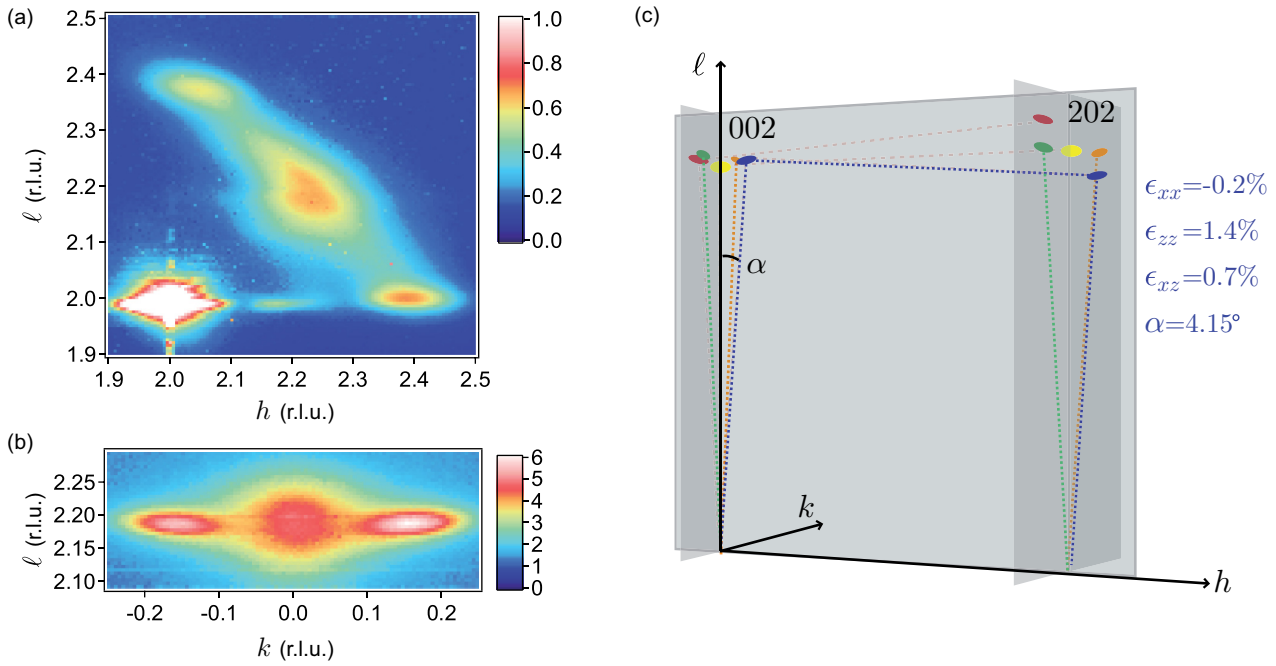

FIG. 7. RSM of sample 8-S. (a) $h\ell$ cut of the reciprocal space in the vicinity of the 202 Ni reflection. (b) ℓk cut of the reciprocal space in the vicinity of the 202 Ni reflection, at $h = 2.225$. (c) Schematic representation of the reciprocal lattice space with 002 and 202 Ni reflections associated to different domains in Ni nanowires. The values of the inclination angle α and of ϵ_{ij} are associated with the variant in dark blue on the sketch.

physical length of the wires and should indeed be compared to the typical length observed for the Moiré patterns axial variation in Fig. 4, of the order of 10–20 nm. The central spot at $h = k = 0$ is much broader both along ℓ and in the $\ell = 2.15$ plane. We do not analyze the profiles for this spot here because it has a composite structure that can be better seen by examining the associated 202 reflection.

Figure 7 shows cuts of the reciprocal space in the vicinity of the 202 Ni reflection. The nonhomogeneity of the central spot can be better appreciated from the slice at $k = 0$ displayed in Fig. 7(a). This spot is composed of an elliptical spot with a long axis oriented at 45° and of a smaller, more symmetric, spot which is less rotated. The counterparts of the four additional spots in the 002 mapping can be identified in the 202 mapping: two spots centered at $h = 2.05$, $\ell = 2.37$ and $h = 2.39$, $\ell = 2.00(5)$ in the $k = 0$ plane, and two symmetrical spots in the $h = 2.225$ plane, shown in Fig. 7(b) located at $\ell = 2.18$, $k = \pm 0.1575$. From such data and mapping of additional reflections (data not shown), the spots can be associated to reflections arising from Ni domains having different strain states and different inclination angle α, α being the angle between the [001] direction of Ni and the [001] of the STO matrix. This is represented schematically in Fig. 7(c). From the position of the spots in reciprocal space, α, ϵ_{xx}, ϵ_{xz}, and ϵ_{zz} can be determined. The composite central spot is associated with diffraction from highly strained domains with $\langle\epsilon_{zz}\rangle = 3.2\%$, $\langle\epsilon_{xx}\rangle = -0.4\%$, and $\epsilon_{xz} = 0$. Among these domains, two families can be distinguished, giving rise to the composite structure of the central spot. The first one consists of domains that are well aligned, with $\alpha = 0$ and have a small coherence length along ℓ. The second one consists of portions of wires with similar strain values, a larger coherence length but characterized by a dispersion of α around 0. This angular disorder gives rise to the elongated structure at 45° in the $k = 0$ cut of the 220 reciprocal map observed in Fig. 7(a). The other spots can be ascribed to four equivalent types of domains that differ only by the direction of inclination ($\pm\alpha$ rotation around [100] or $\pm\alpha$ rotation around [010]). The indexation of diffraction spots is shown in dark blue in Fig. 7(c) for one of the domain types. From the peak position, the strain can be determined. These domains are partially relaxed compared to the aligned one and slightly sheared. We get $\langle\epsilon_{zz}\rangle = 1.4\%$, $\langle\epsilon_{xx}\rangle = -0.2\%$ and $\langle\epsilon_{xz}\rangle = 0.7\%$ and $\alpha = \pm 4.15°$. Associated to this partial strain relaxation, we observe an increase of the axial coherence length ($L_{\text{coh}} = 12.6$ nm) for these domains.

The deduced structure for the NWs, with domains having distinct orientations, is consistent with cross-sectional imaging by TEM. The value of the inclination angle α matches well the one deduced from the Moiré analysis. ϵ_{ij} values indicate that the strain state is peculiar within the Ni domains. The $\epsilon_{xx}/\epsilon_{zz}$ ratio falls well below the Poisson ratio of bulk Ni ($\nu = 0.31$), indicating an expansion of the unit cell volume. This could be a consequence of the constraints imposed by vertical epitaxy, in particular of the fact that in-plane radial relaxation is energetically more favorable than axial relaxation.

The lattice mismatch between Ni (bulk lattice parameter 3.524 Å) and $SrTiO_3$ (bulk lattice parameter 3.905 Å) is quite large. In the present case, we consider the mismatch at the vertical heterointerface between the NWs and the matrix that has an out of plane parameter $c = 3.944$ Å (determined from the fact that the 002 reflection of the matrix has maximal intensity at $\ell = 1.98$).

Considering the domains that are tilted by $|\alpha| = 4.15°$, we will restrict the discussion to the variant indicated in dark blue in Fig. 7(c). The same considerations apply for the

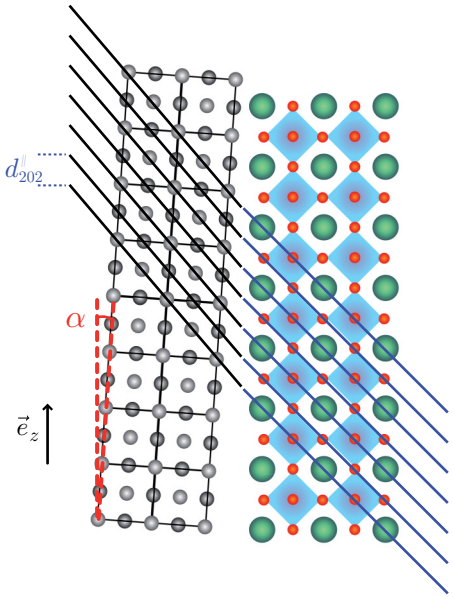

FIG. 8. Sketch of the lattice matching for Ni domains with a 4° misorientation of the [001] direction with respect to the [001] direction of the matrix.

other variants after 90° in-plane rotations that reproduce the fourfold in-plane symmetry of the system. The fact that the 202 reflection associated with the tilted domains is located at $\ell = 2.00(5)$ in reciprocal lattice unit of $SrTiO_3$ indicates that rotation allows us to nearly reach lattice matching of (101) planes along the vertical heterointerface. This is represented schematically in Fig. 8. Let $\vec{g}^{\star}_{202}$ be the reciprocal vector associated with the 202 reflection. The inter-reticular distance viewed along the direction z of the heterointerface, $d^{\parallel}_{202}$ is equal to $1/\vec{g}^{\star}_{202}.\vec{e}_z$.

Since $\vec{g}^{\star}_{202}.\vec{e}_z = 2.00(5)$, we get $d^{\parallel}_{202} = 1.948$ Å, to be compared with $d_{002} = 1.972$ Å for the matrix. It is thus obvious that the tilt allows us to reduce the mismatch drastically by matching (101) planes as sketched in Fig. 8. The mismatch is indeed lowered to 1.2%. It should be noted that simulation of the RSM (see Appendix) indicates that strain relaxation and rotation of the $[001]_{Ni}$ axis occur in a correlated manner.

Considering the aligned domains with $\langle \epsilon_{zz} \rangle = 3.2\%$, the average lattice parameter along z is equal to 3.637 Å; this corresponds to a mismatch of 7.8% that could be accommodated by domain epitaxy with 13 unit cells of Ni matching 12 unit cells of $SrTiO_3$ matrix along z. A possible interpretation of the composite domain structure could be that both matching mechanisms compete and that the energy barrier between these two (meta)stable states can be crossed at the growth temperature. It should be noted that the curved interface between a NW and the matrix in the (001) plane, in absence of fully developed faceting of the NWs, implies that the (101) plane matching cannot be effective on the whole perimeter of the embedded nano-objects. As a result, structural disorder will be generated at the Ni-STO interface and its relative contribution will evidently increase with decreasing NW diameter. In a similar fashion, the coexistence of [001] aligned regions with tilted ones within the NWs implies that a certain volume fraction is occupied by low-angle tilt boundaries. Again, this will

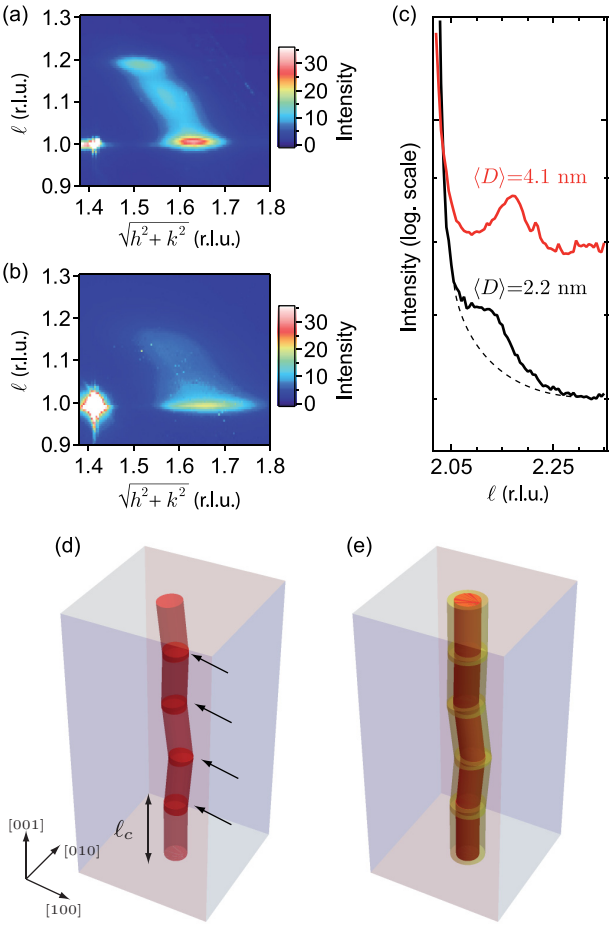

FIG. 9. Vertical-epitaxy-induced disorder in NW composites. (a),(b) (111) maps for two different samples with large difference in NW diameter [$\langle D \rangle = 4.1$ nm in (a), $\langle D \rangle = 2.2$ nm in (b)] reveals large intensity loss for $\langle D \rangle = 2.2$ nm. (c) θ-2θ scans for the same two samples, evidencing the loss of crystalline order along ℓ. (d),(e) Schematic of the Ni-STO interface with tilted Ni domain. (d) Ni crystallite rotation induces creation of low angle GB (marked with arrows); (e) structural disorder might originate at Ni-STO interfaces as well (highlighted in yellow).

be linked to the creation of structurally disordered regions, and the fraction of disordered Ni, related to grain boundary (GB) regions, may increase upon diameter reduction. Indeed, we observe a significant evolution of the diffraction patterns upon reduction of $\langle D \rangle$. As shown in Fig. 9, the diffracted intensity is much weaker for $\langle D \rangle = 2.2$ nm. The composite nature of the diffraction spots is still present and the fact that a sizable portion of the diffracted intensity is located near $\ell = 1$ for the Ni 111 spot indicates that tilt and associated GBs are still present upon diameter reduction. Figures 9(d) and 9(e) give a schematic picture of the sources of crystallographic disorder in the NWs, compatible with the measured diffraction patterns.

D. Grain boundaries, structural disorder, and loss of crystallinity

In order to further quantify the average degree of disorder in the wires and gather information on the local structure of

Ni-STO interfaces as well as Ni-Ni GB regions on an atomic scale, we deepened our structural analysis by performing extensive x-ray absorption measurements at the Ni K edge. A detailed description of the experimental conditions and parameters used for data acquisition has already been given in Sec. II. For data interpretation, raw spectra were first treated with Athena (Ifeffit package) for background removal, deglitching and normalization and Artemis (Ifeffit package) was used for EXAFS analysis and fitting of k^2-weighted $\chi(k)$ data to the standard K-edge EXAFS formula [38]. To achieve maximum consistency, the same analysis procedure was used for all NW samples. First, Ni-foil measurements were employed to determine the amplitude reduction factor resulting from many-body losses. The obtained value of $S_0^2 = 0.80 \pm 0.05$ (setting the number of next neighbors to $N_{\text{n.n}} = 12$) was then taken for all subsequent fits where $N_{\text{n.n}}$, the edge energy correction ΔE_0, the next neighbor distance $R_{\text{n.n}}$, and EXAFS Debye-Waller factor $\sigma^2_{\text{n.n}}$ were used as fit parameters. Within measurement uncertainty, deduced ΔE_0 values obtained on nanocomposite samples were all found compatible with $\Delta E_0(\text{bulk}) = 6.5 \pm 0.9$ eV. Fourier transformations were performed in the range $3\ \text{Å}^{-1} < k < 11\ \text{Å}^{-1}$ using a Hanning window with $dk = 1\ \text{Å}^{-1}$. We restricted all fits to the first coordination shell with $1\,\text{Å} < R < 3\,\text{Å}$. Finally, theoretical XANES spectra were obtained via full multiple scattering FEFF8.0 calculations using a Ni fcc cluster with diameter 1.14 nm, strained along the [001] direction and contracted in plane to achieve volume conservation.

In the following description of our results, we first focus on the near edge structure (XANES) of the measured spectra, resulting from multiple scattering contributions of 1s electrons, as this allows for a qualitative "fingerprinting" analysis of the embedded NWs. Figure 10 shows a survey of data obtained on samples 10-S, 9-S, 7-S, and 6-S. As can clearly be inferred from direct comparison with a Ni-foil reference spectrum, all nanocomposites exhibit a purely metallic signature and the agreement between spectra obtained on the largest nanowires (9-S and 10-S) and bulk data is striking and corroborates EDX results presented in an earlier part of this paper. However, closer analysis of the data reveals small systematic differences between the samples. In fact, with decreasing wire diameter, we observe a progressive flattening of the spectra. Although the overall metallic shape is preserved, a "blurring" of the characteristic peaks B, C, and D becomes apparent. This loss of XANES fine structure, resulting from a reduction of multiple scattering events, is a known signature of disordered or amorphous materials and has been reported in various systems, including matrix-embedded Co and Ge nanoparticles [39,40] or sonochemically-prepared amorphous Fe [41].

Additional evidence for a reduction of crystalline order in the smallest nanowires scrutinized in the present study was obtained by studying the linear dichroic response of the system. Figure 10(b) shows difference spectra $\Delta I = I_\perp - I_\parallel$ obtained by subtraction of XAS data gathered in $\mathcal{L}_\perp$ and $\mathcal{L}_\parallel$ geometry, respectively. With decreasing NW diameter, a clear trend emerges with the gradual appearance of four peaks in the energy window 8320 eV $< E <$ 8400 eV. In sample 4-U for example ($\epsilon_{zz} \approx 3.6\%$), these are located at approximately 8342 eV, 8352 eV, 8362 eV, and 8391 eV, thus close to predicted values obtained from calculated LD spectra on a

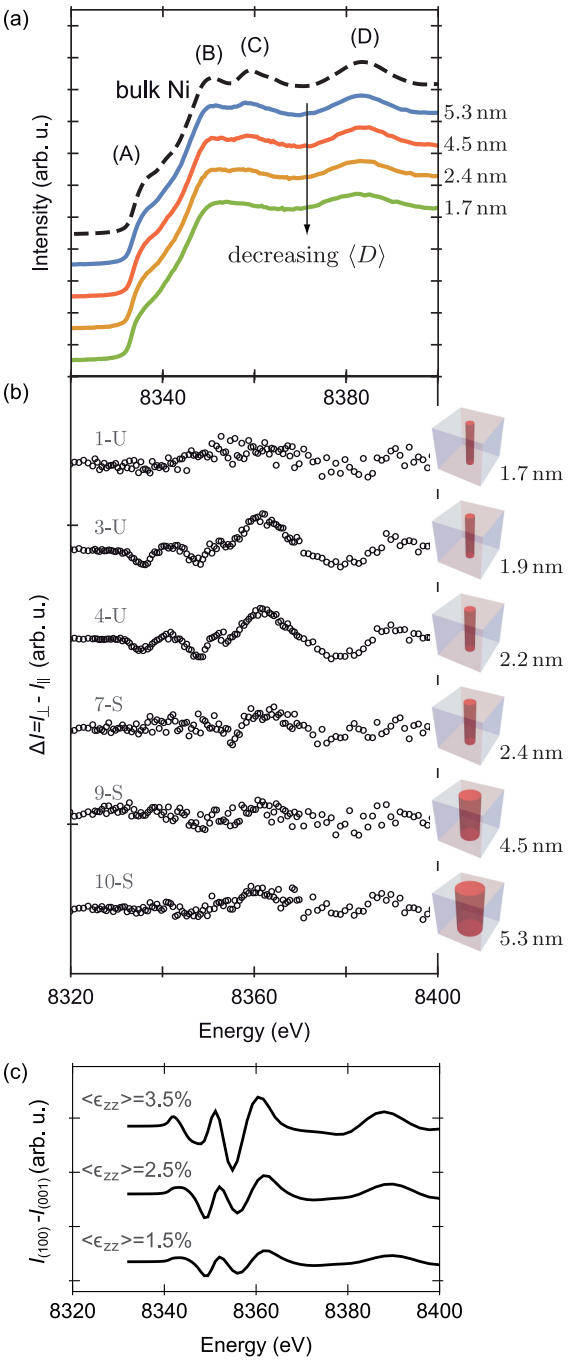

FIG. 10. Measured and simulated Ni K-edge XANES data. (a) XANES spectra for various nanocomposites (samples 6-S, 7-S, 9-S, and 10-S) with decreasing average nanowire diameter $\langle D \rangle$ (top to bottom, all measurements performed in $\mathcal{L}_\parallel$ configuration) and Ni-foil reference data. (b) Linear dichroic signal, i.e., $\Delta I = I_\perp - I_\parallel$ as a function of $\langle D \rangle$. (c) Simulated XANES data as a function of applied strain.

strained fcc cluster with $\epsilon_{zz} = 3.5\%$, as shown in Fig. 10(c), where the maximum values of the oscillations are found at 8341.9 eV, 8351.0 eV, 8360.4 eV and 8387.9 eV, respectively. In addition, we observe the same trend of amplitude increase with strain in our simulations, although the amplitude of the calculated spectra exceeds that of their experimental

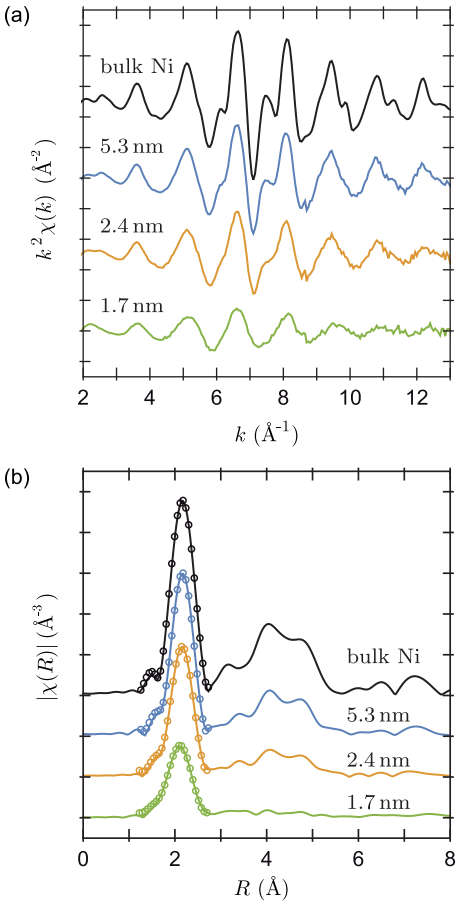

FIG. 11. Measured and fitted Ni K-edge EXAFS data. (a) k^2 weighted $\chi(k)$ spectra ($\mathcal{L}_\parallel$ geometry) as a function of average NW size $\langle D\rangle$ as well as Ni bulk data shown for comparison (samples 10-S, 7-S, and 1-U). (b) Fourier transformed spectra (solid lines) and fits (circles) to the first coordination shell.

counterparts by a factor of roughly three. This discrepancy can be attributed to highly idealized conditions used in our XANES modeling: The clusters present an ideal fcc structure without defects, grain boundaries, and interfaces. Furthermore, the strain distribution has not been taken into account. Taken together, the qualitative agreement between our modeling and experimental data confirms that the measured dichroic signal has its origin in a straining of the wires along their axis. Surprisingly, sample 1-U, which exhibits the smallest $\langle D\rangle$ values scrutinized herein, gets out of line, being characterized by a prominent breakdown of LD. Complete relaxation of the strain appears unlikely, considering the evolution of $\langle\epsilon_{zz}\rangle$ with diameter in all other samples as well as the aforementioned diffraction results. Absence of dichroism rather has to be interpreted as characteristic signature of a pronounced loss of crystalline order, i.e., amorphization of the Ni NWs going hand in hand with a dramatic lowering of the symmetry of the system.

In fact, EXAFS analysis eventually provides reliable quantitative proof for this hypothesis. Figure 11 shows selected k^2-weighted $\chi(k)$ values as a function of NW diameter as well as their FT and fits to the first neighbor shell. Table II presents a summary of the parameters derived from these data. The first unambiguous indication for an increase of structural disorder in the NWs is the increase of σ^2 when $\langle D\rangle$ is successively reduced, which holds true for both configurations scrutinized herein. Indeed, this parameter accounts for the mean square variation in mean path lengths (in a Gaussian approximation to the pair distribution function) [42]. As all measurements were performed at room temperature, an increase of structural disorder must be responsible for the augmentation of σ^2 and we highlight that the highest values described herein compare well with those obtained on amorphous, SiO_2-embedded metallic Co nanoclusters with average diameters $\langle D\rangle < 4$ nm [39]. Final and decisive evidence for a complete loss of crystalline order eventually results from an analysis of FT spectra shown in Fig. 11(b) which goes beyond the first coordination shell. While for the Ni foil, as well as for all samples with $\langle D\rangle > 1.7$ nm, the second and third shell contributions can clearly be evidenced, the FT spectrum of sample 1-U flattens almost entirely for $R > 3$ Å which demonstrates the breakdown of crystallinity in this sample. We stress that a similar solid state amorphization has been observed earlier in layered systems with large lattice mismatch. Indeed, in planar Gd/Fe and Y/Fe heterostructures, a critical thickness $t_c = 2.3 \pm 0.1$ nm was reported, below which the Fe layers lost their crystalline structure [43,44].

The exact nature of the induced disorder remains unclear though. EXAFS data unveils a strong reduction of the coordination number, which cannot be explained by an increase of the fraction of Ni atoms located at metal-oxide interfaces alone. In fact, it is well known that the Gaussian approximation commonly used in basic EXAFS fitting breaks down for large disorder and induces an artificial reduction of N and R [42]. Indeed, in the present study, we are also confronted with a small decrease of R which clearly correlates with the observed changes in coordination number. Cumulant-expansion correction terms, accounting for asymmetric and/or broadened distance distributions can fix the issue in the case of moderate disorder [45]. For large structural disorder however, this approach fails and one has to stick to *ad-hoc* chosen pair distribution functions $g(r)$ in order to circumvent the aforementioned problems. Over the years, a variety of asymmetric radial distribution functions have been proposed and applied with success to the description of amorphous systems [41,46,47].

In the present case, we did not achieve any significant improvement of our fits by using additional cumulants (C_3 and C_4). Calculated values of the third cumulant on NW samples reach rather large maximum values around 3×10^{-4} Å^{-3}, but no systematic evolution of C_3 with $\langle D\rangle$ could be evidenced. Additionally, only minor corrections of R were achieved and N did not increase significantly. Fits with an additional fourth cumulant chosen as a floating parameter were generally of poor quality. An additional attempt was undertaken to use strongly asymmetric $g(r)$ functions [42] using Viper [48]. While in this approach, increased values of R and N close to bulk values were achieved; the general quality of the fits was not as good as in the simple Gaussian case. This casts doubt on our choice of $g(r)$ and might reflect the difficulty to adequately describe a superposition of contributions from crystalline and disordered parts of the sample.

TABLE II. Ni K-edge EXAFS fit parameters for measurements on Ni-STO nanocomposites (in $\mathcal{L}_\perp$ and $\mathcal{L}_\parallel$ configuration) as well as bulk Ni reference.

Sample	$\langle D \rangle$ (nm)	$N_\parallel$	$N_\perp$	$R_\parallel$ (Å)	$R_\perp$ (Å)	$\sigma^2_\parallel$ (10^{-3} Å^2)	$\sigma^2_\perp$ (10^{-3} Å^2)
1-U	1.7	7.1 ± 0.7	6.9 ± 0.9	2.448 ± 0.007	2.438 ± 0.011	10.5 ± 1.0	10.4 ± 1.2
3-U	1.9	7.6 ± 0.5	6.7 ± 0.7	2.459 ± 0.005	2.431 ± 0.007	9.6 ± 0.7	8.9 ± 1.0
4-U	2.2	8.5 ± 0.5	8.3 ± 0.7	2.463 ± 0.005	2.442 ± 0.006	9.1 ± 0.6	9.1 ± 0.8
5-U	2.5	8.0 ± 0.8	7.5 ± 1.2	2.473 ± 0.007	2.455 ± 0.011	9.2 ± 0.9	8.7 ± 1.5
6-S	1.7	9.2 ± 0.5	8.6 ± 0.6	2.465 ± 0.004	2.457 ± 0.006	9.9 ± 0.6	9.5 ± 0.7
7-S	2.4	10.0 ± 0.6	10.0 ± 0.7	2.479 ± 0.004	2.473 ± 0.005	8.0 ± 0.5	8.3 ± 0.7
9-S	4.5	10.6 ± 0.5	10.8 ± 1.0	2.477 ± 0.003	2.471 ± 0.005	6.8 ± 0.4	6.9 ± 0.9
10-S	5.3	10.6 ± 0.5	10.7 ± 0.8	2.484 ± 0.003	2.475 ± 0.006	6.6 ± 0.4	6.8 ± 0.6
Ni foil	bulk	12 ± 0.4		2.482 ± 0.004		5.5 ± 0.5	

Finally, alternative mechanisms inducing a lowering of the coordination number might also be conceived. On one hand, the exact behavior of Ni atoms located at (or in close vicinity to) the interface is difficult to grasp when relying on the information gathered in the present study. While the formation of NiO bonds appears unlikely considering our EXAFS fits (we do not find evidence for significant intermixing at the Ni-STO interface), the structure of the Ni interface layer might deviate from that of bulk amorphous materials, presenting, for example, a lower packing density, or even a gaslike random atomic arrangement, as has been proposed in previous work on GB in nanocrystalline materials [49]. On the other hand, it appears clearly that the growth strategy used in our work promotes the creation of vacancies in the composite thin film. The STO matrix is strongly oxygen deficient, which becomes apparent in XRD data, where an out of plane increase of the lattice parameter is observed. During growth, the STO matrix acts as a reducing agent, soaking up oxygen and thereby promoting the formation of metallic Ni. Oxygen atoms incorporated in the wires during growth will thus eventually diffuse into the oxide matrix. In this picture, the nanowires act as point vacancy sinks, an effect which should increase, with increasing oxygen deficiency of the matrix. In fact, this hypothesis is supported by our data: Direct comparison of samples 1-U and 6-S or 5-U and 7-S, grown under UHV and HV conditions, respectively, reveals pronounced differences in coordination number, although they both display similar average axial strain states $\langle \epsilon_{zz} \rangle$ and almost identical NW diameters. Averaging the coordination numbers obtained in $\mathcal{L}_\perp$ and $\mathcal{L}_\parallel$ geometries, listed in Table II, we get a mean coordination number $N \simeq 7$ for sample 1-U, to be compared to $N \simeq 9$ for sample 6-S with comparable diameter. The same trend is observed when comparing sample 5-U ($N \simeq 8$) and sample 7-S ($N \simeq 10$). We therefore conclude that the gradual loss of crystalline structure of the nanowires when decreasing $\langle D \rangle$ not only results from the large Ni-STO interfacial lattice mismatch and progressive intrinsic GB creation via domain rotation, but is also significantly promoted by vacancy incorporation, further weakening the stability of the fcc lattice.

IV. CONCLUSION

In the present work, we combined state of the art XRD, HRTEM, and XAS measurements to analyze the structure of ultrathin, vertically epitaxied, Ni nanowires embedded in $SrTiO_3/SrTiO_3(001)$. Our data show that the nanowires experience large, diameter dependent axial strains and permit us to unveil a partial strain relaxation mechanism, which consists of a gradual coherent rotation of domains in order to achieve (110) lattice plane matching between the NWs and the matrix. The classical picture of a straight, monolithic embedded nanopillar thus turns out to be an oversimplification, missing crucial structural details characteristic of vertical epitaxy in systems with large lattice mismatch. In fact, Ni NWs have to be conceived as a sequence of stacked, strained, and tilted crystalline building blocks, with a typical length of approximately 10–20 nm. While creation of these smaller entities reduces the elastic energy of the system, it goes hand in hand with the appearance of grain boundaries. This relaxation pathway is thus inherently associated with a decrease of crystalline order. When reducing the size of the NWs, the relative amount of disordered NW atoms increases, which was clearly evidenced *via* quantitative EXAFS analysis. For the smallest diameters, grain boundary and heterointerface induced disorder becomes dominant and finally results in a complete loss of crystalline order. This shows that vertical epitaxy cannot be understood by simply recycling concepts known from planar epitaxy. In these systems, the presence of free surfaces allows for effective strain relaxation. In Ni-STO nanocolumnar composites, the presence of large heterointerfaces imposes more severe structural constraints.

From an application point of view, this can be exploited to tune specific properties of the embedded nanowires, such as magnetic anisotropy. Indeed, the axial strain will induce an extra magnetoelastic anisotropy contribution, scaling as $\langle \epsilon_{zz} \rangle$ and proportional to the magnetostriction coefficient [27,50]. As the mean axial strain increases upon diameter reduction, the control of $\langle D \rangle$ provides a lever to act on the magnetic properties of the nanocomposite. This, however, as demonstrated herein, cannot be extrapolated for too thin diameters where a partial or even complete crystalline to amorphous transition will act as a key limiting factor.

Finally, we emphasize that, although the present study has exclusively focused on Ni-STO composites the strain relaxation mechanism described in this paper may well be ubiquitous in vertically assembled epitaxial metal-oxide nanostructures, particularly for systems with cube-on-cube epitaxial relationships. In Ni NWs assemblies in CeO_2 with cube-

on-cube epitaxy, a diameter-dependent axial strain, lower than the lattice mismatch, exists [28] and slight crystalline misorientations are frequent. We also have recently observed the same tilted epitaxy in Co_xNi_{1-x} NWs in $SrTiO_3$ and (Sr, Ba)TiO_3 matrices, which suggests that our results can be generalized to alloy nanowires. For pure Co nanowires in CeO_2 with hexagonal close packed (hcp) and face-centered cubic (fcc) structures competing, stacking faults and hcp-fcc phase coexistence may contribute to strain relaxation and complicate the crystalline microstructure. To what extent the present findings also apply to bcc metals in vertical epitaxy [6,51], or even more complex 3D epitaxial architectures [52], is currently under investigation.

ACKNOWLEDGMENTS

This study was supported by the French SOLEIL synchrotron through two proposals (proposal numbers 20160182 and 20161095). The authors thank the SOLEIL staff for smoothly running the facility. Dr. A. Resta of the SOLEIL SixS beamline is kindly acknowledged for introducing us to the use of the Binoculars software and XRD data processing. The authors also gratefully thank S. Chenot for his assistance during the installation of the PLD and his precious skills in UHV-related issues, S. Hidki for diffraction measurements, F. Breton for his assistance and design of the PLD control system, and J.-M. Guigner, IMPMC, CNRS-UPMC, for access to the TEM facilities. The STEM studies were carried out on the Titan Themis microscope acquired as part of the "TEMPOS" project (ANR-10-EQPX-0050). This work was supported by French state funds managed by the Agence Nationale de la Recherche within the Investissements d'Avenir programme under reference ANR-11-IDEX-0004-02, and more specifically within the framework of the Cluster of Excellence MATISSE led by Sorbonne Universités. M.H. acknowledges financial support from the French Embassy in Berlin (Service pour la Science et la Technologie) and Campus France. X.W. gratefully acknowledges financial support of the Chinese Government Scholarship from China Scholarship Council (CSC No. 201608070062).

APPENDIX: SIMULATION OF THE RECIPROCAL SPACE MAPPINGS

Diffraction intensity from the NWs can be simulated within the framework of the kinematic theory of x-ray diffraction. We performed calculations in order to ensure that the main structural features deduced from the experimental data for sample 8-S are indeed sufficient to reproduce the reciprocal space maps (RSM) satisfactorily. Expected reciprocal space maps were established with assemblies of coherent domains of Ni NWs of 4 nm diameter and 6 or 12 nm length corresponding to the order of the coherence lengths measured. Furthermore, considering specific RSM such as $h0\ell$ maps involve only x and z components of the atomic displacements, thereby simplifying the 3D problem to the 2D one.

The $h0\ell$ RSM around 002 and 202 spots were satisfactorily simulated by considering three distinct contributions. The first one is related to highly strained domains with a Gaussian distribution of axial strain ($\langle\epsilon_{zz}\rangle = 3.5\%$, full width at half maximum 1.2%), with $[001]_{Ni} \parallel [001]_{STO}$. The contribution of such domains in the RSM is indicated by thick black ellipses in Figs. 12(a) and 12(c). Their coherence length is estimated to be 6 nm. The two other contributions arise from portions of the wires where $[001]_{Ni}$ is misoriented by an angle α with respect to $[001]_{STO}$. The distribution of domains as a function of α has a first maximum around 0° and another one around $\alpha_0 = 4.15°$, four times degenerated, corresponding to clockwise and anticlockwise rotations around $[100]_{STO}$ and $[010]_{STO}$. In such domains, the strain is correlated to the misorientation α and can be described in the form:

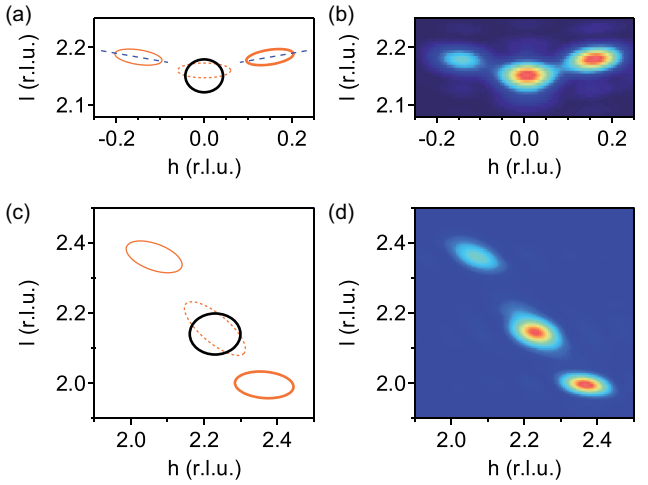

FIG. 12. (a),(b) $h0\ell$ map of the reciprocal space in the vicinity of the 002 Ni reflection: (a) schematics of the RSM, (b) simulation of the RSM. (c),(d) $h0\ell$ map of the reciprocal space in the vicinity of the 202 Ni reflection: (c) schematics of the RSM, (d) simulation of the RSM.

$$\epsilon_{zz} = \epsilon^0_{zz} + \beta_{zz}(\alpha/\alpha_0)^2 \quad \text{(A1)}$$

$$\epsilon_{xx} = \epsilon^0_{xx} + \beta_{xx}(\alpha/\alpha_0)^2 \quad \text{(A2)}$$

$$\epsilon_{xz} = \epsilon_{zx} = \beta_{xz}(\alpha/\alpha_0) \quad \text{(A3)}$$

with $\epsilon^0_{zz} = +3.0\%$, $\epsilon^0_{xx} = -0.4\%$, $\beta_{zz} = -1.6\%$, $\beta_{xx} = +0.2\%$, and $\beta_{xz} = -0.7\%$. ϵ^0_{zz} and ϵ^0_{xx} are the axial tensile and radial compressive strains, respectively, for the nontilted domains. Negative β_{zz} and positive β_{xx} coefficients represent the relaxation rates of the axial and radial strains, respectively, versus the misorientation α, for the tilted domains. The slight shear component in tilted domains is reflected by the coefficient β_{xz}.

Such a relationship between the strain and misorientation in the domains, together with the domain distribution, reproduces well the positions of the diffraction spots. However, the intensities and notably the bending of the diffraction spots are not correctly calculated. This indicates that the model of a uniform strain field inside each coherent domain is too simplistic and suggests the existence of internal distortion inside domains. In a phenomenological way, a random internal distortion with respect to the previous uniform strain field is added inside each coherent domain. Taking the center of one domain as reference, the random atomic displacements δu_z

and δu_x over the spatial coordinates z and x in the domain are parameterized by one random variable $\delta\omega$ as follows:

$$\delta u_z = \left(x + 2z\beta_{zz}\alpha/\alpha_0^2\right)\delta\omega \tag{A4}$$

$$\delta u_x = \left(2x\beta_{xx}\alpha/\alpha_0^2 - z\right)\delta\omega. \tag{A5}$$

The standard deviation of $\delta\omega$ is chosen to be 0.007. Such an ingredient allows us to reproduce satisfactorily the bending of the diffraction spots related to the portions with α at 0° and around ±4°, bending symbolized by dashed and solid red ellipses, respectively, in Figs. 12(a) and 12(c).

Finally, the effect of the incidence angle is taken into account for the RSM of 002 which was obtained in the specular geometry. For the RSM of 202, the measurement was made at constant grazing incidence of 0.3 degree. Calculated mappings are shown in Figs. 12(b) and 12(d). The agreement with the experimental RSM is quite good, as can be seen by comparison with Figs. 5 and 7. The intensity asymmetry for the spots with α around ±4° in the RSM of 002 in Fig. 12(b) is entirely explained by the incidence effect or the irradiated surface of the sample. For the RSM of 202, the intensity asymmetry for the spots with α around ±4° is mainly determined by the internal distortion.

From these simulations, we extract the characteristics of NWs, namely the values of $\langle\epsilon_{zz}\rangle$, $\langle\epsilon_{xx}\rangle$, and $\langle\epsilon_{xz}\rangle$ for both straight and tilted sections, and we infer the correlation between relaxation of strain and tilt of the lattice. More precisely, the NWs axial tensile strain relaxes when the lattice planes rotate around Ni [100] (or [010]) axis, until achieving a (101) lattice plane match between the NWs and matrix.

[1] K. J. Choi, M. Biegalski, Y. L. Li, A. Sharan, J. Schubert, R. Uecker, P. Reiche, Y. B. Chen, X. Q. Pan, V. Gopalan, L.-Q. Chen, D. G. Schlom, and C. B. Eom, Science **306**, 1005 (2004).

[2] H. Wang, C. Du, P. C. Hammel, and F. Yang, Phys. Rev. B **89**, 134404 (2014).

[3] C. Du, R. Adur, H. Wang, A. J. Hauser, F. Yang, and P. C. Hammel, Phys. Rev. Lett. **110**, 147204 (2013).

[4] I. Bozovic, G. Logvenov, I. Belca, B. Narimbetov, and I. Sveklo, Phys. Rev. Lett. **89**, 107001 (2002).

[5] H. Zheng, J. Wang, L. Mohaddes-Ardabili, M. Wuttig, L. Salamanca-Riba, D. G. Schlom, and R. Ramesh, Appl. Phys. Lett. **85**, 2035 (2004).

[6] L. Mohaddes-Ardabili, H. Zheng, S. B. Ogale, B. Hannoyer, W. Tian, J. Wang, S. E. Lofland, S. R. Shinde, T. Zhao, Y. Jia, L. Salamanca-Riba, D. G. Schlom, M. Wuttig, and R. Ramesh, Nat. Mater. **3**, 533 (2004).

[7] H. Zheng, J. Wang, S. E. Lofland, Z. Ma, L. Mohaddes-Ardabili, T. Zhao, L. Salamanca-Riba, S. R. Shinde, S. B. Ogale, F. Bai *et al.*, Science **303**, 661 (2004).

[8] H. Zheng, Q. Zhan, F. Zavaliche, M. Sherburne, F. Straub, M. P. Cruz, L.-Q. Chen, U. Dahmen, and R. Ramesh, Nano Lett. **6**, 1401 (2006).

[9] Q. Zhan, R. Yu, S. P. Crane, H. Zheng, C. Kisielowski, and R. Ramesh, Appl. Phys. Lett. **89**, 172902 (2006).

[10] J. L. MacManus-Driscoll, P. Zerrer, H. Wang, H. Yang, J. Yoon, A. Fouchet, R. Yu, M. G. Blamire, and Q. Jia, Nat. Mater. **7**, 314 (2008).

[11] Z. Bi, J. H. Lee, H. Yang, Q. Jia, J. L. MacManus-Driscoll, and H. Wang, J. Appl. Phys. **106**, 094309 (2009).

[12] A. Chen, Z. Bi, H. Hazariwala, X. Zhang, Q. Su, L. Chen, Q. Jia, J. L. MacManus-Driscoll, and H. Wang, Nanotechnology **22**, 315712 (2011).

[13] N. M. Aimon, D. H. Kim, H. K. Choi, and C. A. Ross, Appl. Phys. Lett. **100**, 092901 (2012).

[14] N. Dix, R. Muralidharan, J.-M. Rebled, S. Estradé, F. Peiró, M. Varela, J. Fontcuberta, and F. Sánchez, ACS Nano **4**, 4955 (2010).

[15] J. L. MacManus-Driscoll, Adv. Funct. Mater. **20**, 2035 (2010).

[16] W. Zhang, A. Chen, Z. Bi, Q. Jia, J. L. MacManus-Driscoll, and H. Wang, Curr. Opin. Solid State Mater. Sci. **18**, 6 (2014).

[17] J. Huang, J. L. MacManus-Driscoll, and H. Wang, J. Mater. Res. **32**, 4054 (2017).

[18] J. MacManus-Driscoll, A. Suwardi, A. Kursumovic, Z. Bi, C.-F. Tsai, H. Wang, Q. Jia, and O. J. Lee, APL Materials **3**, 062507 (2015).

[19] A. Chen, J.-M. Hu, P. Lu, T. Yang, W. Zhang, L. Li, T. Ahmed, E. Enriquez, M. Weigand, Q. Su, H. Wang, J.-X. Zhu, J. L. MacManus-Driscoll, L.-Q. Chen, D. Yarotski, and Q. Jia, Sci. Adv. **2**, e1600245 (2016).

[20] S. M. Yang, S. B. Lee, J. Jian, W. Zhang, Q. X. Jia, H. Wang, T. W. Noh, S. V. Kalinin, and J. L. MacManus-Driscoll, Nat. Commun. **6**, 8588 (2015).

[21] F. Vidal, Y. Zheng, J. Milano, D. Demaille, P. Schio, E. Fonda, and B. Vodungbo, Appl. Phys. Lett. **95**, 152510 (2009).

[22] P. Schio, F. Vidal, Y. Zheng, J. Milano, E. Fonda, D. Demaille, B. Vodungbo, J. Varalda, A. J. A. de Oliveira, and V. H. Etgens, Phys. Rev. B **82**, 094436 (2010).

[23] F. Vidal, Y. Zheng, P. Schio, F. J. Bonilla, M. Barturen, J. Milano, D. Demaille, E. Fonda, A. J. A. de Oliveira, and V. H. Etgens, Phys. Rev. Lett. **109**, 117205 (2012).

[24] P. Schio, F. J. Bonilla, Y. Zheng, D. Demaille, J. Milano, A. J. A. de Oliveira, and F. Vidal, J. Phys.: Condens. Matter **25**, 056002 (2013).

[25] P. Schio, M. Barturen, J. Milano, F. J. Bonilla, Y. Zheng, F. Vidal, and A. J. A. de Oliveira, Mater. Res. Express **1**, 035015 (2014).

[26] A. Novikova, E. Fonda, Y. Dumont, Y. Zheng, D. Demaille, and F. Vidal, J. Phys. D: Appl. Phys. **48**, 235001 (2015).

[27] F. J. Bonilla, A. Novikova, F. Vidal, Y. Zheng, E. Fonda, D. Demaille, V. Schuler, A. Coati, A. Vlad, Y. Garreau, M. Sauvage-Simkin, Y. Dumont, S. Hidki, and V. H. Etgens, ACS Nano **7**, 4022 (2013).

[28] V. Schuler, F. J. Bonilla, D. Demaille, A. Coati, A. Vlad, Y. Garreau, M. Sauvage-Simkin, A. Novikova, E. Fonda, S. Hidki, V. Etgens, F. Vidal, and Y. Zheng, Nano Research **8**, 1964 (2015).

[29] V. Schuler, J. Milano, A. Coati, A. Vlad, M. Sauvage-Simkin, Y. Garreau, D. Demaille, S. Hidki, A. Novikova, E. Fonda, Y. Zheng, and F. Vidal, Nanotechnology **27**, 495601 (2016).

[30] M. Hennes, V. Schuler, X. Weng, J. Buchwald, D. Demaille, Y. Zheng, and F. Vidal, Nanoscale **10**, 7666 (2018).
[31] A. A. Stashkevich, Y. Roussigné, A. N. Poddubny, S.-M. Chérif, Y. Zheng, F. Vidal, I. V. Yagupov, A. P. Slobozhanyuk, P. A. Belov, and Y. S. Kivshar, Phys. Rev. B **92**, 214436 (2015).
[32] Y. Roussigné, S. M. Chérif, A. A. Stashkevich, F. Vidal, and Y. Zheng, J. Appl. Phys. **118**, 233903 (2015).
[33] K. van Benthem, C. Scheu, W. Sigle, and M. Rühle, Z. Metallkd. **93**, 362 (2002).
[34] R. Winter, P. Shekhter, K. Tang, L. Floreano, A. Verdini, P. C. McIntyre, and M. Eizenberg, ACS Appl. Mater. Interf. **8**, 16979 (2016).
[35] T. Suzuki, Y. Nishi, and M. Fujimoto, Philos. Mag. A **80**, 621 (2000).
[36] T. Ohnishi, K. Shibuya, T. Yamamoto, and M. Lippmaa, J. Appl. Phys. **103**, 103703 (2008).
[37] C. M. Brooks, L. F. Kourkoutis, T. Heeg, J. Schubert, D. A. Muller, and D. G. Schlom, Appl. Phys. Lett. **94**, 162905 (2009).
[38] B. Ravel and M. Newville, J. Synchrotron Radiat. **12**, 537 (2005).
[39] D. J. Sprouster, R. Giulian, L. L. Araujo, P. Kluth, B. Johannessen, N. Kirby, K. Nordlund, and M. C. Ridgway, Phys. Rev. B **81**, 155414 (2010).
[40] L. L. Araujo, R. Giulian, D. J. Sprouster, C. S. Schnohr, D. J. Llewellyn, P. Kluth, D. J. Cookson, G. J. Foran, and M. C. Ridgway, Phys. Rev. B **78**, 094112 (2008).
[41] G. J. Long, D. Hautot, Q. A. Pankhurst, D. Vandormael, F. Grandjean, J. P. Gaspard, V. Briois, T. Hyeon, and K. S. Suslick, Phys. Rev. B **57**, 10716 (1998).
[42] B. K. Teo, *EXAFS: Basic Principles and Data Analysis* (Springer-Verlag, Berlin, Heidelberg, 1986).
[43] J. Landes, Ch. Sauer, B. Kabius, and W. Zinn, Phys. Rev. B **44**, 8342 (1991).
[44] S. Handschuh, J. Landes, U. Koebler, Ch. Sauer, G. Kisters, A. Fuss, and W. Zinn, J. Magn. Magn. Mater. **119**, 254 (1993).
[45] G. Bunker, *Introduction to EXAFS* (Cambridge University Press, Cambridge, 2010).
[46] E. D. Crozier and A. J. Seary, Can. J. Phys. **58**, 1388 (1980).
[47] B. K. Teo, H. S. Chen, R. Wang, and M. R. Antonio, J. Non-Cryst. Solids **58**, 249 (1983).
[48] K. V. Klementev, J. Phys. D: Appl. Phys. **34**, 209 (2001).
[49] T. Haubold, R. Birringer, B. Lengeler, and H. Gleiter, Phys. Lett. A **135**, 461 (1989).
[50] H. Zheng, J. Kreisel, Y.-H. Chu, R. Ramesh, and L. Salamanca-Riba, Appl. Phys. Lett. **90**, 113113 (2007).
[51] T. Goto, D. H. Kim, X. Sun, M. C. Onbasli, J. M. Florez, S. P. Ong, P. Vargas, K. Ackland, P. Stamenov, N. M. Aimon, M. Inoue, H. L. Tuller, G. F. Dionne, J. M. D. Coey, and C. A. Ross, Phys. Rev. Applied **7**, 024006 (2017).
[52] X. Sun, J. Huang, J. Jian, M. Fan, H. Wang, Q. Li, J. L. Mac Manus-Driscoll, P. Lu, X. Zhang, and H. Wang, Mater. Horiz. **5**, 536 (2018).